1. PASSAGE OF PARTICLES THROUGH MATTER

Revised January 2012 by H. Bichsel (University of Washington), D.E. Groom (LBNL), and S.R. Klein (LBNL).

1.1. Notation

Table 1.1: Summary of variables used in this section. The kinematic variables β and γ have their usual meanings.

Symbol	Definition	Units or Value
α	Fine structure constant $(e^2/4\pi\epsilon_0\hbar c)$	$1/137.035\,999\,11(46)$
M	Incident particle mass	MeV/c^2
E	Incident part. energy γMc^2	MeV
T	Kinetic energy	MeV
$m_e c^2$	Electron mass $\times\ c^2$	$0.510\,998\,918(44)$ MeV
r_e	Classical electron radius $e^2/4\pi\epsilon_0 m_e c^2$	$2.817\,940\,325(28)$ fm
N_A	Avogadro's number	$6.022\,1415(10) \times 10^{23}$ mol^{-1}
ze	Charge of incident particle	
Z	Atomic number of absorber	
A	Atomic mass of absorber	g mol^{-1}
K/A	$4\pi N_A r_e^2 m_e c^2/A$	$0.307\,075$ MeV g^{-1} cm^2 for A = 1 g mol^{-1}
I	Mean excitation energy	eV (*Nota bene!*)
$\delta(\beta\gamma)$	Density effect correction to ionization energy loss	
$\hbar\omega_p$	Plasma energy $(\sqrt{4\pi N_e r_e^3}\ m_e c^2/\alpha)$	$\sqrt{\rho\,\langle Z/A\rangle} \times 28.816$ eV (ρ in g cm^{-3})
N_e	Electron density	(units of r_e)$^{-3}$
w_j	Weight fraction of the jth element in a compound or mixture	
n_j	$\propto$ number of jth kind of atoms in a compound or mixture	
—	$4\alpha r_e^2 N_A/A$	$(716.408$ g cm$^{-2})^{-1}$ for $A = 1$ g mol^{-1}
X_0	Radiation length	g cm^{-2}
E_c	Critical energy for electrons	MeV
$E_{\mu c}$	Critical energy for muons	GeV
E_s	Scale energy $\sqrt{4\pi/\alpha}\, m_e c^2$	21.2052 MeV
R_M	Molière radius	g cm^{-2}

1.2. Electronic energy loss by heavy particles [1–34]

1.2.1. *Moments and cross sections*:

The electronic interactions of fast charged particles with speed $v = \beta c$ occur in *single collisions with energy losses* E [1], leading to ionization, atomic, or collective excitation. Most frequently the energy losses are small (for 90% of all collisions the energy losses are less than 100 eV). In thin absorbers few collisions will take place and the total energy loss will show a large variance [1]; also see Sec. 1.2.7 below. For particles with charge ze more massive than electrons ("heavy"

particles), scattering from free electrons is adequately described by the Rutherford differential cross section [2], * †

$$\frac{d\sigma_R\,(E;\beta)}{dE} = \frac{2\pi r_e^2 m_e c^2 z^2}{\beta^2}\,\frac{\left(1-\beta^2 E/T_{\max}\right)}{E^2}\ , \tag{1.1}$$

where $T_{\max}$ is the maximum energy transfer possible in a single collision. But in matter electrons are not free. E must be finite and depends on atomic and bulk structure. For electrons bound in atoms Bethe [3] used "Born Theorie" to obtain the differential cross section

$$\frac{d\sigma_B\,(E;\beta)}{dE} = \frac{d\sigma_R\,(E,\beta)}{dE} B\,(E)\ . \tag{1.2}$$

Examples of $B(E)$ and $d\sigma_B/dE$ can be seen in Figs. 5 and 6 of Ref. 1.

Bethe's theory extends only to some energy above which atomic effects were not important. The free-electron cross section (Eq. (1.1)) can be used to extend the cross section to $T_{\max}$. At high energies σ_B is further modified by polarization of the medium, and this "density effect," discussed in Sec. 1.2.4, must also be included. Less important corrections are discussed below.

The mean number of collisions with energy loss between E and $E + dE$ occurring in a distance δx is $N_e \delta x\,(d\sigma/dE)dE$, where $d\sigma(E;\beta)/dE$ contains all contributions. It is convenient to define the moments

$$M_j\,(\beta) = N_e\,\delta x \int E^j \frac{d\sigma\,(E;\beta)}{dE} dE\ , \tag{1.3}$$

so that M_0 is the mean number of collisions in δx, M_1 is the mean energy loss in δx, $M_2 - M_1^2$ is the variance, *etc.* The number of collisions is Poisson-distributed with mean M_0. N_e is either measured in electrons/g ($N_e = N_A Z/A$) or electrons/cm^3 ($N_e = N_A\,\rho Z/A$). The former is used throughout this chapter, since quantities of interest (dE/dx, X_0, *etc.*) vary smoothly with composition when there is no density dependence.

* For spin 0 particles. The β dependence in the parentheses is different for spin 1/2 and spin 1 particles, but it is not important except at energies far above atomic binding energies.

† In high-energy physics E normally means total energy, $T + mc^2$. In stopping power discussions, E means kinetic energy, and we follow that convention (with some inconsistency).

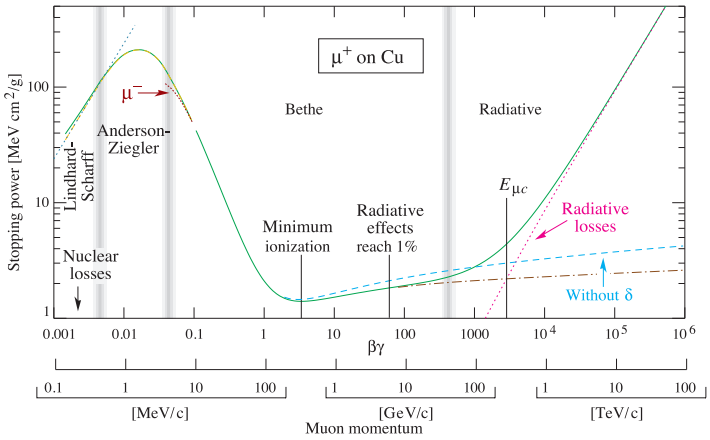

Fig. 1.1: Stopping power ($= \langle -dE/dx \rangle$) for positive muons in copper as a function of $\beta\gamma = p/Mc$ over nine orders of magnitude in momentum (12 orders of magnitude in kinetic energy). Solid curves indicate the total stopping power. Data below the break at $\beta\gamma \approx 0.1$ are taken from ICRU 49 [4], and data at higher energies are from Ref. 5. Vertical bands indicate boundaries between different approximations discussed in the text. The short dotted lines labeled "μ^-" illustrate the "Barkas effect," the dependence of stopping power on projectile charge at very low energies [6].

1.2.2. *Stopping power at intermediate energies*:

The mean rate of energy loss by moderately relativistic charged heavy particles, $M_1/\delta x$, is well-described by the "Bethe" equation,

$$-\left\langle \frac{dE}{dx} \right\rangle = Kz^2 \frac{Z}{A}\frac{1}{\beta^2}\left[\frac{1}{2}\ln\frac{2m_e c^2\beta^2\gamma^2 T_{\max}}{I^2} - \beta^2 - \frac{\delta(\beta\gamma)}{2}\right] . \quad (1.4)$$

It describes the mean rate of energy loss in the region $0.1 \lesssim \beta\gamma \lesssim 1000$ for intermediate-Z materials with an accuracy of a few %. With the symbol definitions and values given in Table 1.1, the units are MeV g^{-1}cm^2. At the lower limit the projectile velocity becomes comparable to atomic electron "velocities" (Sec. 1.2.3), and at the upper limit radiative effects begin to be important (Sec. 1.6). Both limits are Z dependent. Here $T_{\max}$ is the maximum kinetic energy which can be imparted to a free electron in a single collision, and the other variables are defined in Table 1.1. A minor dependence on M at the highest energies is introduced through $T_{\max}$, but for all practical purposes $\langle dE/dx \rangle$ in a given material is a function of β alone.

For heavy projectiles, like ions, additional terms are required to account for higher-order photon coupling to the target, and to account for the finite size of the target radius. These can change dE/dx by a factor of two or more for the heaviest nuclei in certain kinematic regimes [7].

Few concepts in high-energy physics are as misused as $\langle dE/dx \rangle$. The main problem is that the mean is weighted by very rare events with large single-collision energy deposits. Even with samples of hundreds of events a dependable value for the mean energy loss cannot be obtained. Far better and more easily measured is the most probable energy loss, discussed in Sec. 1.2.7. The most probable energy loss in a detector is considerably below the mean given by the Bethe equation.

In a TPC (Sec. 31.6.5), the mean of 50%–70% of the samples with the smallest signals is often used as an estimator.

Although it must be used with cautions and caveats, $\langle dE/dx \rangle$ as described in Eq. (1.4) still forms the basis of much of our

understanding of energy loss by charged particles. Extensive tables are available[5,4, pdg.lbl.gov/AtomicNuclearProperties/].

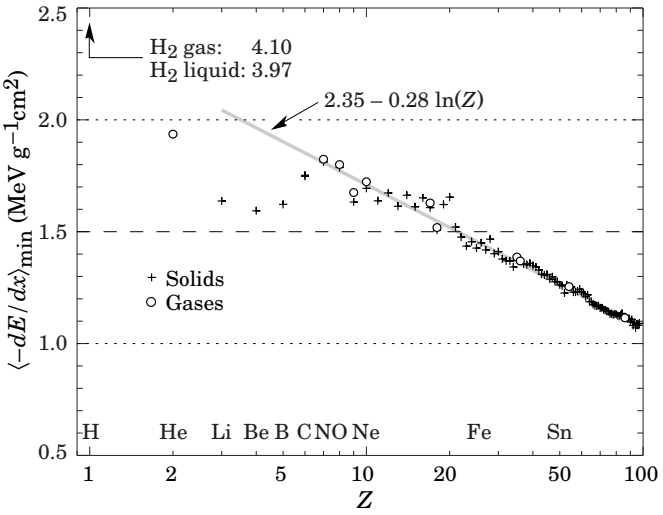

Figure 1.2: Stopping power at minimum ionization for the chemical elements. The straight line is fitted for $Z > 6$. A simple functional dependence on Z is not to be expected, since $\langle -dE/dx \rangle$ also depends on other variables.

The function as computed for muons on copper is shown as the "Bethe" region of Fig. 1.1. Mean energy loss behavior below this region is discussed in Sec. 1.2.3, and the radiative effects at high energy are discussed in Sec. 1.6. Only in the Bethe region is it a function of β alone; the mass dependence is more complicated elsewhere. The stopping power in several other materials is shown in Fig. 27.3. Except in hydrogen, particles with the same velocity have similar rates of energy loss in different materials, although there is a slow decrease in the rate of energy loss with increasing Z. The qualitative behavior difference at high energies between a gas (He in the figure) and the other materials shown in the figure is due to the density-effect correction, $\delta(\beta\gamma)$, discussed in Sec. 1.2.4. The stopping power functions are characterized by broad minima whose position drops from $\beta\gamma = 3.5$ to 3.0 as Z goes from 7 to 100. The values of minimum ionization as a function of atomic number are shown in Fig. 1.2.

In practical cases, most relativistic particles (*e.g.*, cosmic-ray muons) have mean energy loss rates close to the minimum; they are "minimum-ionizing particles," or mip's.

Eq. (1.4) may be integrated to find the total (or partial) "continuous slowing-down approximation" (CSDA) range R for a particle which loses energy only through ionization and atomic excitation. Since dE/dx depends only on β, R/M is a function of E/M or pc/M. In practice, range is a useful concept only for low-energy hadrons ($R \lesssim \lambda_I$, where λ_I is the nuclear interaction length), and for muons below a few hundred GeV (above which radiative effects dominate). R/M as a function of $\beta\gamma = p/Mc$ is shown for a variety of materials in Fig. 1.4.

The mass scaling of dE/dx and range is valid for the electronic losses described by the Bethe equation, but not for radiative losses, relevant only for muons and pions.

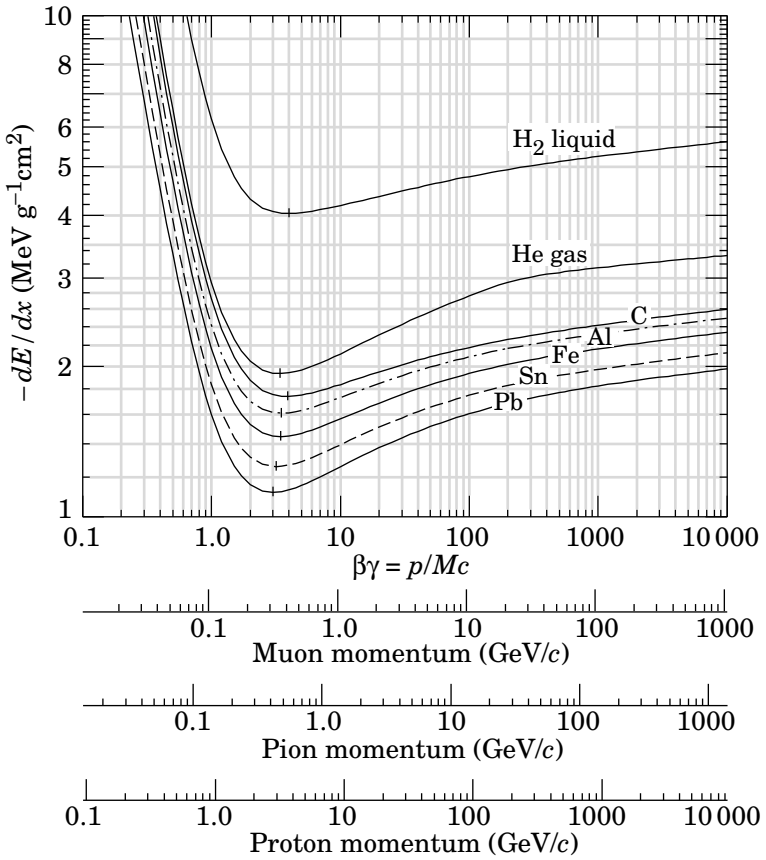

Figure 1.3: Mean energy loss rate in liquid (bubble chamber) hydrogen, gaseous helium, carbon, aluminum, iron, tin, and lead. Radiative effects, relevant for muons and pions, are not included. These become significant for muons in iron for $\beta\gamma \gtrsim 1000$, and at lower momenta in higher-Z absorbers. See Fig. 1.22.

For a particle with mass M and momentum $M\beta\gamma c$, $T_{\rm max}$ is given by

$$T_{\rm max} = \frac{2m_e c^2\,\beta^2\gamma^2}{1 + 2\gamma m_e/M + (m_e/M)^2}\ . \tag{1.5}$$

In older references [2,8] the "low-energy" approximation $T_{\rm max} = 2m_e c^2\,\beta^2\gamma^2$, valid for $2\gamma m_e/M \ll 1$, is often implicit. For a pion in copper, the error thus introduced into dE/dx is greater than 6% at 100 GeV. Structure function corrections to Eq. (1.5) have been considered in the case of incident pions by J.D. Jackson [9], with the conculsion that the effects are negligible below energies in which radiative effects dominate (see Sec. 1.6).

Estimates of the mean excitation energy based on experimental stopping-power measurements for protons, deuterons, and alpha particles are given in ICRU 37 [11].

1.2.4. ***Density effect***: As the particle energy increases, its electric field flattens and extends, so that the distant-collision contribution to Eq. (1.4) increases as $\ln\beta\gamma$. However, real media become polarized, limiting the field extension and effectively truncating this part of the

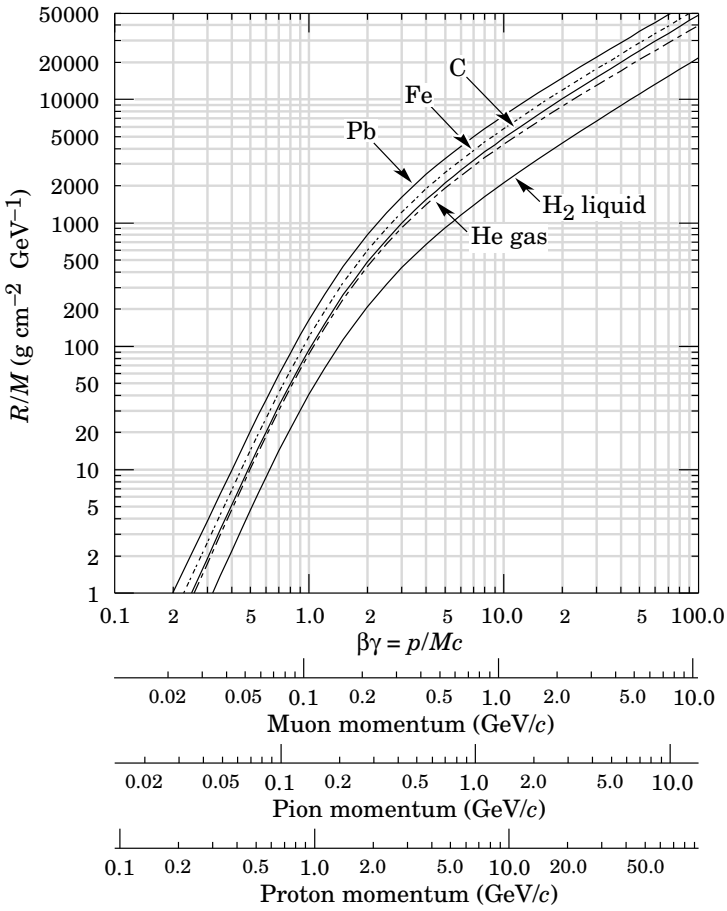

Figure 1.4: Range of heavy charged particles in liquid (bubble chamber) hydrogen, helium gas, carbon, iron, and lead. For example: For a K^+ whose momentum is 700 MeV/c, $\beta\gamma = 1.42$. For lead we read $R/M \approx 396$, and so the range is 195 g cm^{-2}.

logarithmic rise [2–8,19–21]. At very high energies,

$$\delta/2 \to \ln\left(\hbar\omega_p/I\right) + \ln\beta\gamma - 1/2\ , \tag{1.7}$$

where $\delta(\beta\gamma)/2$ is the density effect correction introduced in Eq. (1.4) and $\hbar\omega_p$ is the plasma energy defined in Table 1.1. A comparison with Eq. (1.4) shows that $|dE/dx|$ then grows as $\ln\beta\gamma$ rather than $\ln\beta^2\gamma^2$, and that the mean excitation energy I is replaced by the plasma energy $\hbar\omega_p$. Since the plasma frequency scales as the square root of the electron density, the correction is much larger for a liquid or solid than for a gas, as is illustrated by the examples in Fig. 1.3.

The remaining relativistic rise comes from the $\beta^2\gamma^2$ growth of $T_{\rm max}$, which in turn is due to (rare) large energy transfers to a few electrons. When these events are excluded, the energy deposit in an absorbing layer approaches a constant value, the Fermi plateau (see Sec. 1.2.6 below). At extreme energies (*e.g.*, $>$ 332 GeV for muons in iron, and at a considerably higher energy for protons in iron), radiative effects are more important than ionization losses. These are especially relevant for high-energy muons, as discussed in Sec. 1.6.

1.2.5. ***Energetic knock-on electrons (δ rays)***: The distribution of secondary electrons with kinetic energies $T \gg I$ is [2]

$$\frac{d^2N}{dTdx} = \frac{1}{2}\,Kz^2\frac{Z}{A}\,\frac{1}{\beta^2}\,\frac{F\,(T)}{T^2} \tag{1.8}$$

for $I \ll T \leq T_{\rm max}$, where $T_{\rm max}$ is given by Eq. (1.5). Here β is the velocity of the primary particle. The factor F is spin-dependent, but is about unity for $T \ll T_{\rm max}$. For spin-0 particles $F(T) = (1 - \beta^2 T/T_{\rm max})$; forms for spins 1/2 and 1 are also given by Rossi [2](Sec. 2.3, Eqns. 7 and 8). For incident electrons, the indistinguishability of projectile and target means that the range of T extends only to half the kinetic energy of the incident particle. Additional formulae are given in Ref. 23. Equation (1.8) is inaccurate for T close to I [24].

δ rays of even modest energy are rare. For a $\beta \approx 1$ particle, for example, on average only one collision with $T_e > 10$ keV will occur along a path length of 90 cm of Ar gas [1].

A δ ray with kinetic energy T_e and corresponding momentum p_e is produced at an angle θ given by

$$\cos\theta = (T_e/p_e)\,(p_{\rm max}/T_{\rm max})\ , \tag{1.9}$$

where $p_{\rm max}$ is the momentum of an electron with the maximum possible energy transfer $T_{\rm max}$.

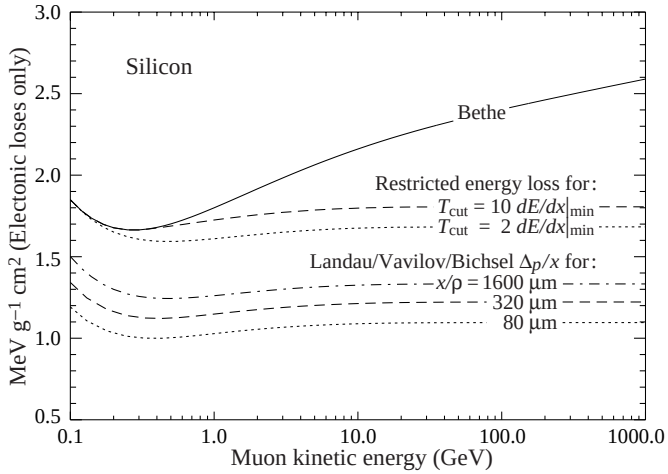

Figure 1.6: Bethe dE/dx, two examples of restricted energy loss, and the Landau most probable energy per unit thickness in silicon. The change of Δ_p/x with thickness x illustrates its $a \ln x + b$ dependence. Minimum ionization ($dE/dx|_{\rm min}$) is 1.664 MeV g^{-1} cm^2. Radiative losses are excluded. The incident particles are muons.

1.2.6. ***Restricted energy loss rates for relativistic ionizing particles***: Further insight can be obtained by examining the mean energy deposit by an ionizing particle when energy transfers are restricted to $T \leq T_{\rm cut} \leq T_{\rm max}$. The restricted energy loss rate is

$$-\left.\frac{dE}{dx}\right|_{T<T_{\rm cut}} = Kz^2\frac{Z}{A}\frac{1}{\beta^2}\left[\frac{1}{2}\ln\frac{2m_ec^2\beta^2\gamma^2T_{\rm cut}}{I^2} - \frac{\beta^2}{2}\left(1+\frac{T_{\rm cut}}{T_{\rm max}}\right) - \frac{\delta}{2}\right]. \tag{1.10}$$

This form approaches the normal Bethe function (Eq. (1.4)) as $T_{\rm cut} \to T_{\rm max}$. It can be verified that the difference between Eq. (1.4) and Eq. (1.10) is equal to $\int_{T_{\rm cut}}^{T_{\rm max}} T(d^2N/dTdx)dT$, where $d^2N/dTdx$ is given by Eq. (1.8).

Since $T_{\rm cut}$ replaces $T_{\rm max}$ in the argument of the logarithmic term of Eq. (1.4), the $\beta\gamma$ term producing the relativistic rise in the close-collision part of dE/dx is replaced by a constant, and $|dE/dx|_{T<T_{\rm cut}}$ approaches the constant "Fermi plateau." (The density effect correction δ eliminates the explicit $\beta\gamma$ dependence produced by the distant-collision contribution.) This behavior is illustrated in Fig. 1.6, where restricted loss rates for two examples of $T_{\rm cut}$ are shown in comparison with the full Bethe dE/dx and the Landau-Vavilov most probable energy loss (to be discussed in Sec. 1.2.7 below).

1.2.7. ***Fluctuations in energy loss***: For detectors of moderate thickness x (*e.g.* scintillators or LAr cells),* the energy loss probability distribution $f(\Delta; \beta\gamma, x)$ is adequately described by the highly-skewed Landau (or Landau-Vavilov) distribution [25,26]. The most probable energy loss is [27]

$$\Delta_p = \xi \left[\ln \frac{2mc^2\beta^2\gamma^2}{I} + \ln \frac{\xi}{I} + j - \beta^2 - \delta\left(\beta\gamma\right) \right] , \qquad (1.11)$$

where $\xi = (K/2)\left\langle Z/A \right\rangle (x/\beta^2)$ MeV for a detector with a thickness x in g cm^{-2}, and $j = 0.200$ [27]. † While dE/dx is independent of thickness, Δ_p/x scales as $a \ln x + b$. The density correction $\delta(\beta\gamma)$ was not included in Landau's or Vavilov's work, but it was later included by Bichsel [27]. The high-energy behavior of $\delta(\beta\gamma)$ (Eq. (1.7)) is such that

$$\Delta_p \underset{\beta\gamma \gtrsim 100}{\longrightarrow} \xi \left[\ln \frac{2mc^2\xi}{\left(\hbar\omega_p\right)^2} + j \right] . \qquad (1.12)$$

Thus the Landau-Vavilov most probable energy loss, like the restricted energy loss, reaches a Fermi plateau. The Bethe dE/dx and Landau-Vavilov-Bichsel Δ_p/x in silicon are shown as a function of muon energy in Fig. 1.6. The energy deposit in the 1600 μm case is roughly the same as in a 3 mm thick plastic scintillator.

The distribution function for the energy deposit by a 10 GeV muon going through a detector of about this thickness is shown in Fig. 1.7. In this case the most probable energy loss is 62% of the mean $(M_1(\langle\Delta\rangle)/M_1(\infty))$. Folding in experimental resolution displaces the peak of the distribution, usually toward a higher value. 90% of the collisions $(M_1(\langle\Delta\rangle)/M_1(\infty))$ contribute to energy deposits below the mean. It is the very rare high-energy-transfer collisions, extending to $T_{\rm max}$ at several GeV, that drives the mean into the tail of the distribution. *The mean of the energy loss given by the Bethe equation, Eq. (*1.4*), is thus ill-defined experimentally and is not useful for describing energy loss by single particles.** It rises as $\ln\beta\gamma$ because $T_{\rm max}$ increases as $\beta^2\gamma^2$. The large single-collision energy transfers that increasingly extend the long tail are rare, making the mean of an

* $G \lesssim 0.05$–0.1, where G is given by Rossi [Ref. 2, Eq. 2.7.10]. It is Vavilov's κ [26].

† Rossi [2], Talman [28], and others give somewhat different values for j. The most probable loss is not sensitive to its value.

* It does find application in dosimetry, where only bulk deposit is relevant.

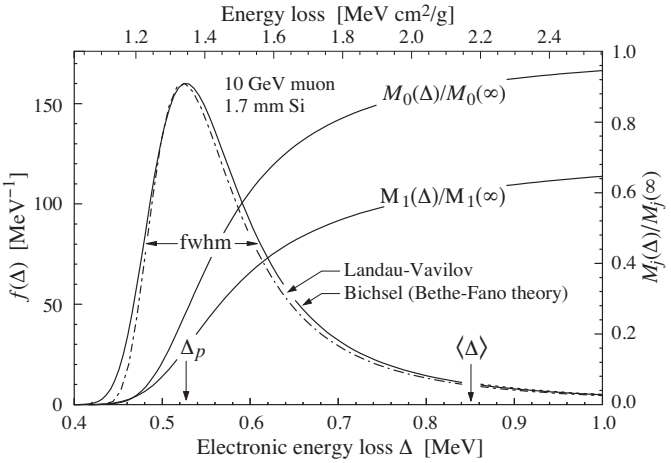

Figure 1.7: Electronic energy deposit distribution for a 10 GeV muon traversing 1.7 mm of silicon, the stopping power equivalent of about 0.3 cm of PVC scintillator [1,13,29]. The Landau-Vavilov function (dot-dashed) uses a Rutherford cross section without atomic binding corrections but with a kinetic energy transfer limit of $T_{\max}$. The solid curve was calculated using Bethe-Fano theory. $M_0(\Delta)$ and $M_1(\Delta)$ are the cumulative 0th moment (mean number of collisions) and 1st moment (mean energy loss) in crossing the silicon. (See Sec. 1.2.1. The fwhm of the Landau-Vavilov function is about 4ξ for detectors of moderate thickness. Δ_p is the most probable energy loss, and $\langle\Delta\rangle$ divided by the thickness is the Bethe $\langle dE/dx\rangle$.

experimental distribution consisting of a few hundred events subject to large fluctuations and sensitive to cuts. *The most probable energy loss should be used.*†

The Landau distribution fails to describe energy loss in thin absorbers such as gas TPC cells [1] and Si detectors [27], as shown clearly in Fig. 1 of Ref. 1 for an argon-filled TPC cell. Also see Talman [28]. While Δ_p/x may be calculated adequately with Eq. (1.11), the distributions are significantly wider than the Landau width $w = 4\xi$ [Ref. 27, Fig. 15]. Examples for 500 MeV pions incident on thin silicon detectors are shown in Fig. 1.8. For very thick absorbers the distribution is less skewed but never approaches a Gaussian.

The most probable energy loss, scaled to the mean loss at minimum ionization, is shown in Fig. 1.9 for several silicon detector thicknesses.

1.2.8. ***Energy loss in mixtures and compounds***: A mixture or compound can be thought of as made up of thin layers of pure elements in the right proportion (Bragg additivity). In this case,

$$\frac{dE}{dx} = \sum w_j \left.\frac{dE}{dx}\right|_j , \tag{1.13}$$

where $dE/dx|_j$ is the mean rate of energy loss (in MeV g cm^{-2}) in the jth element. Eq. (1.4) can be inserted into Eq. (1.13) to find expressions for $\langle Z/A\rangle$, $\langle I\rangle$, and $\langle\delta\rangle$; for example, $\langle Z/A\rangle = \sum w_j Z_j/A_j =$

† An alternative approach is taken in TPC analysis, where some fraction of the highest energy deposit signals along a track, *e.g.* 20%, are discarded before taking the average.

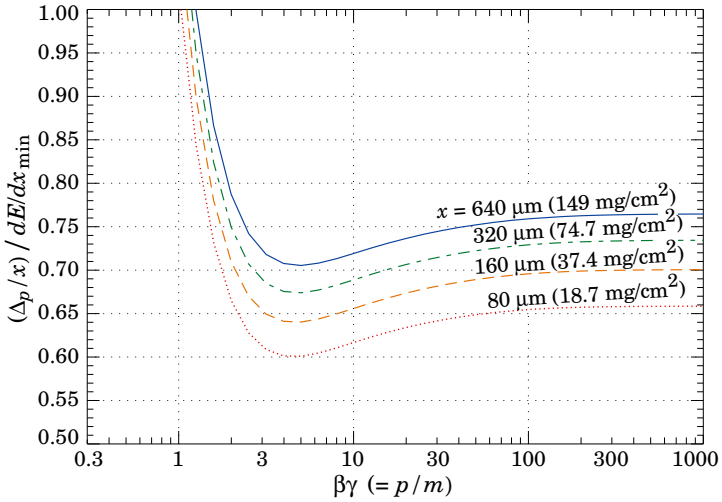

Figure 1.9: Most probable energy loss in silicon, scaled to the mean loss of a minimum ionizing particle, 388 eV/μm (1.66 MeV g^{-1}cm^2).

$\sum n_j Z_j / \sum n_j A_j$. However, $\langle I \rangle$ as defined this way is an underestimate, because in a compound electrons are more tightly bound than in the free elements, and $\langle \delta \rangle$ as calculated this way has little relevance, because it is the electron density that matters. If possible, one uses the tables given in Refs. 21 and 30, or the recipes given in Ref. 22 (repeated in Ref. 5), which include effective excitation energies and interpolation coefficients for calculating the density effect correction.

1.3. Multiple scattering through small angles

A charged particle traversing a medium is deflected by many small-angle scatters. Most of this deflection is due to Coulomb scattering from nuclei, and hence the effect is called multiple Coulomb scattering. (However, for hadronic projectiles, the strong interactions also contribute to multiple scattering.) The Coulomb scattering distribution is well represented by the theory of Molière [35]. It is roughly Gaussian for small deflection angles, but at larger angles (greater than a few θ_0, defined below) it behaves like Rutherford scattering, with larger tails than does a Gaussian distribution.

If we define

$$\theta_0 = \theta^{\rm rms}_{\rm plane} = \frac{1}{\sqrt{2}}\,\theta^{\rm rms}_{\rm space}\ . \tag{1.14}$$

then it is sufficient for many applications to use a Gaussian approximation for the central 98% of the projected angular distribution, with a width given by [36,37]

$$\theta_0 = \frac{13.6\ {\rm MeV}}{\beta cp}\ z\ \sqrt{x/X_0}\Big[1 + 0.038 \ln\left(x/X_0\right)\Big]\ . \tag{1.15}$$

Here p, βc, and z are the momentum, velocity, and charge number of the incident particle, and x/X_0 is the thickness of the scattering medium in radiation lengths (defined below). This value of θ_0 is from a fit to Molière distribution for singly charged particles with $\beta = 1$ for all Z, and is accurate to 11% or better for $10^{-3} < x/X_0 < 100$.

Eq. (1.15) describes scattering from a single material, while the usual problem involves the multiple scattering of a particle traversing many different layers and mixtures. Since it is from a fit to a Molière distribution, it is incorrect to add the individual θ_0 contributions in

quadrature; the result is systematically too small. It is much more accurate to apply Eq. (1.15) once, after finding x and X_0 for the combined scatterer.

1.4. Photon and electron interactions in matter

1.4.1. ***Radiation length***: High-energy electrons predominantly lose energy in matter by bremsstrahlung, and high-energy photons by e^+e^- pair production. The characteristic amount of matter traversed for these related interactions is called the radiation length X_0, usually measured in g cm^{-2}. It is both (a) the mean distance over which a high-energy electron loses all but $1/e$ of its energy by bremsstrahlung, and (b) $\frac{7}{9}$ of the mean free path for pair production by a high-energy photon [39]. It is also the appropriate scale length for describing high-energy electromagnetic cascades. X_0 has been calculated and tabulated by Y.S. Tsai [40]:

$$\frac{1}{X_0} = 4\alpha r_e^2 \frac{N_A}{A}\left\{ Z^2 \left[L_{\rm rad} - f\left(Z\right) \right] + Z\, L'_{\rm rad} \right\} . \tag{1.23}$$

For $A = 1$ g mol^{-1}, $4\alpha r_e^2 N_A/A = (716.408$ g cm$^{-2})^{-1}$. $L_{\rm rad}$ and $L'_{\rm rad}$ are given in Table 1.2. The function $f(Z)$ is an infinite sum, but for elements up to uranium can be represented to 4-place accuracy by

$$f\left(Z\right) = a^2 \left[\left(1 + a^2\right)^{-1} + 0.20206 \right.$$
$$\left. -0.0369\, a^2 + 0.0083\, a^4 - 0.002\, a^6 \right] , \tag{1.24}$$

where $a = \alpha Z$ [41].

Table 1.2: Tsai's $L_{\rm rad}$ and $L'_{\rm rad}$, for use in calculating the radiation length in an element using Eq. (1.23).

Element	Z	$L_{\rm rad}$	$L'_{\rm rad}$
H	1	5.31	6.144
He	2	4.79	5.621
Li	3	4.74	5.805
Be	4	4.71	5.924
Others	> 4	$\ln(184.15\, Z^{-1/3})$	$\ln(1194\, Z^{-2/3})$

The radiation length in a mixture or compound may be approximated by

$$1/X_0 = \sum w_j/X_j \ , \tag{1.25}$$

where w_j and X_j are the fraction by weight and the radiation length for the jth element.

1.4.2. ***Energy loss by electrons***: At low energies electrons and positrons primarily lose energy by ionization, although other processes (Møller scattering, Bhabha scattering, e^+ annihilation) contribute, as shown in Fig. 1.12. While ionization loss rates rise logarithmically with energy, bremsstrahlung losses rise nearly linearly (fractional loss is nearly independent of energy), and dominates above a few tens of MeV in most materials (See Sec. 1.4.3 below.)

Ionization loss by electrons and positrons differ somewhat, and both differ from loss by heavy particles because of the kinematics, spin, and the identity of the incident electron with the electrons which it ionizes. Complete discussions and tables can be found in Refs. 10, 11, and 30.

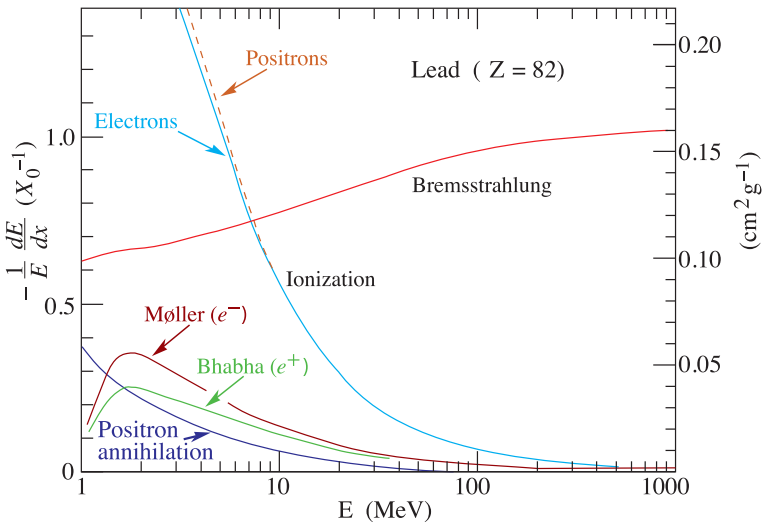

Figure 1.12: Fractional energy loss per radiation length in lead as a function of electron or positron energy. Electron (positron) scattering is considered as ionization when the energy loss per collision is below 0.255 MeV, and as Møller (Bhabha) scattering when it is above. Adapted from Fig. 3.2 from Messel and Crawford, *Electron-Photon Shower Distribution Function Tables for Lead, Copper, and Air Absorbers*, Pergamon Press, 1970. Messel and Crawford use $X_0(\mathrm{Pb}) = 5.82$ g/cm^2, but we have modified the figures to reflect the value given in the Table of Atomic and Nuclear Properties of Materials ($X_0(\mathrm{Pb}) = 6.37$ g/cm^2).

At very high energies and except at the high-energy tip of the bremsstrahlung spectrum, the cross section can be approximated in the "complete screening case" as [40]

$$d\sigma/dk = (1/k)\,4\alpha r_e^2 \{ \left(\tfrac{4}{3} - \tfrac{4}{3}y + y^2\right) \left[Z^2\left(L_{\mathrm{rad}} - f\left(Z\right)\right) + Z\,L'_{\mathrm{rad}}\right] + \tfrac{1}{9}\left(1-y\right)\left(Z^2+Z\right) \} \ , \tag{1.27}$$

where $y = k/E$ is the fraction of the electron's energy transfered to the radiated photon. At small y (the "infrared limit") the term on the second line ranges from 1.7% (low Z) to 2.5% (high Z) of the total. If it is ignored and the first line simplified with the definition of X_0 given in Eq. (1.23), we have

$$\frac{d\sigma}{dk} = \frac{A}{X_0 N_A k}\left(\tfrac{4}{3} - \tfrac{4}{3}y + y^2\right) \ . \tag{1.28}$$

This formula is accurate except in near $y = 1$, where screening may become incomplete, and near $y = 0$, where the infrared divergence is removed by the interference of bremsstrahlung amplitudes from nearby scattering centers (the LPM effect) [42,43] and dielectric suppression [44,45]. These and other suppression effects in bulk media are discussed in Sec. 1.4.5.

Except at these extremes, and still in the complete-screening approximation, the number of photons with energies between k_{min} and k_{max} emitted by an electron travelling a distance $d \ll X_0$ is

$$N_\gamma = \frac{d}{X_0}\left[\frac{4}{3}\ln\left(\frac{k_{\mathrm{max}}}{k_{\mathrm{min}}}\right) - \frac{4\left(k_{\mathrm{max}} - k_{\mathrm{min}}\right)}{3E} + \frac{k_{\mathrm{max}}^2 - k_{\mathrm{min}}^2}{2E^2}\right] \ . \tag{1.29}$$

1.4.3. ***Critical energy***: An electron loses energy by bremsstrahlung at a rate nearly proportional to its energy, while the ionization loss rate varies only logarithmically with the electron energy. The *critical energy* E_c is sometimes defined as the energy at which the two loss rates are equal [47]. Among alternate definitions is that of Rossi [2], who defines the critical energy as the energy at which the ionization loss per radiation length is equal to the electron energy. Equivalently, it is the same as the first definition with the approximation $|dE/dx|_{\rm brems} \approx E/X_0$. This form has been found to describe transverse electromagnetic shower development more accurately (see below).

The accuracy of approximate forms for E_c has been limited by the failure to distinguish between gases and solid or liquids, where there is a substantial difference in ionization at the relevant energy because of the density effect. Separate fits to $E_c(Z)$, using the Rossi definition, have been made with functions of the form $a/(Z+b)^\alpha$, but α was found to be essentially unity. Since E_c also depends on A, I, and other factors, such forms are at best approximate.

Values of E_c for both electrons and positrons in more than 300 materials can be found at `pdg.lbl.gov/AtomicNuclearProperties`.

1.4.4. ***Energy loss by photons***: Contributions to the photon cross section in a light element (carbon) and a heavy element (lead) are shown in Fig. 1.16. At low energies it is seen that the photoelectric effect dominates, although Compton scattering, Rayleigh scattering, and photonuclear absorption also contribute. The photoelectric cross section is characterized by discontinuities (absorption edges) as thresholds for photoionization of various atomic levels are reached. Photon attenuation lengths for a variety of elements are shown in Fig. 30.16, and data for 30 eV$< k <$100 GeV for all elements is available from the web pages given in the caption. Here k is the photon energy.

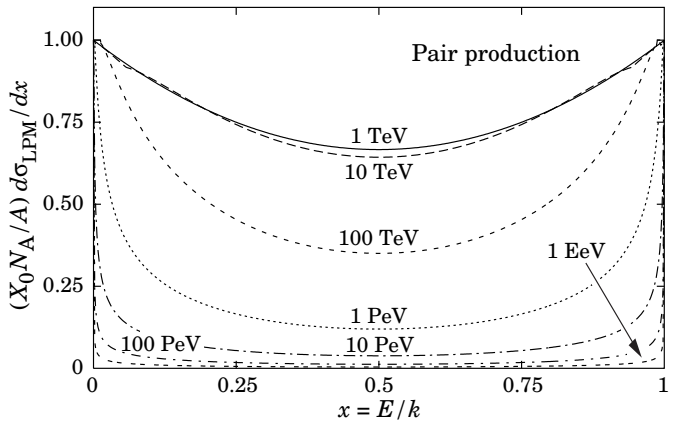

Figure 1.18: The normalized pair production cross section $d\sigma_{LPM}/dy$, versus fractional electron energy $x = E/k$.

The increasing domination of pair production as the energy increases is shown in Fig. 1.17 of the full *Review*. Using approximations similar to those used to obtain Eq. (1.28), Tsai's formula for the differential cross section [40] reduces to

$$\frac{d\sigma}{dx} = \frac{A}{X_0 N_A}\left[1 - \tfrac{4}{3}x\,(1-x)\right] \tag{1.30}$$

in the complete-screening limit valid at high energies. Here $x = E/k$ is the fractional energy transfer to the pair-produced electron (or positron), and k is the incident photon energy. The cross section is very closely related to that for bremsstrahlung, since the Feynman diagrams are variants of one another. The cross section is of necessity symmetric between x and $1 - x$, as can be seen by the solid curve in Fig. 1.18 of the full *Review*. See the review by Motz, Olsen, & Koch for a more detailed treatment [50].

Eq. (1.30) may be integrated to find the high-energy limit for the total e^+e^- pair-production cross section:

$$\sigma = \tfrac{7}{9}\,(A/X_0 N_A)\ . \tag{1.31}$$

Equation Eq. (1.31) is accurate to within a few percent down to energies as low as 1 GeV, particularly for high-Z materials.

1.4.5. ***Bremsstrahlung and pair production at very high energies***: At ultrahigh energies, Eqns. 1.27–1.31 will fail because of quantum mechanical interference between amplitudes from different scattering centers. Since the longitudinal momentum transfer to a given center is small ($\propto k/E(E-k)$, in the case of bremsstrahlung), the interaction is spread over a comparatively long distance called the formation length ($\propto E(E-k)/k$) via the uncertainty principle. In alternate language, the formation length is the distance over which the highly relativistic electron and the photon "split apart." The interference is usually destructive. Calculations of the "Landau-Pomeranchuk-Migdal" (LPM) effect may be made semi-classically based on the average multiple scattering, or more rigorously using a quantum transport approach [42,43].

In amorphous media, bremsstrahlung is suppressed if the photon energy k is less than $E^2/(E + E_{LPM})$ [43], where*

$$E_{LPM} = \frac{\left(m_e c^2\right)^2 \alpha X_0}{4\pi\hbar c\rho} = (7.7\ \text{TeV/cm}) \times \frac{X_0}{\rho}\ . \tag{1.32}$$

Since physical distances are involved, X_0/ρ, in cm, appears. The energy-weighted bremsstrahlung spectrum for lead, $k\,d\sigma_{LPM}/dk$, is shown in Fig. 1.13 of the full *Review*. With appropriate scaling by X_0/ρ, other materials behave similarly.

For photons, pair production is reduced for $E(k-E) > k\,E_{LPM}$. The pair-production cross sections for different photon energies are shown in Fig. 1.18 of the full *Review*.

If $k \ll E$, several additional mechanisms can also produce suppression. When the formation length is long, even weak factors can perturb the interaction. For example, the emitted photon can coherently forward scatter off of the electrons in the media. Because of this, for $k < \omega_p E/m_e \sim 10^{-4}$, bremsstrahlung is suppressed by a factor $(km_e/\omega_p E)^2$ [45]. Magnetic fields can also suppress bremsstrahlung. In crystalline media, the situation is more complicated, with coherent enhancement or suppression

1.4.6. ***Photonuclear and electronuclear interactions at still higher energies***: At still higher photon and electron energies, where the bremsstrahlung and pair production cross-sections are heavily suppressed by the LPM effect, photonuclear and electronuclear interactions predominate over electromagnetic interactions.

* This definition differs from that of Ref. 51 by a factor of two. E_{LPM} scales as the 4th power of the mass of the incident particle, so that $E_{LPM} = (1.4 \times 10^{10}\ \text{TeV/cm}) \times X_0/\rho$ for a muon.

At photon energies above about 10^{20} eV, for example, photons usually interact hadronically. The exact cross-over energy depends on the model used for the photonuclear interactions. At still higher energies ($\gtrsim 10^{23}$ eV), photonuclear interactions can become coherent, with the photon interaction spread over multiple nuclei. Essentially, the photon coherently converts to a ρ^0, in a process that is somewhat similar to kaon regeneration [53]. These processes are illustrated in Fig. 30.19.

Similar processes occur for electrons. As electron energies increase and the LPM effect suppresses bremsstrahlung, electronuclear interactions become more important. At energies above 10^{21}eV, these electronuclear interactions dominate electron energy loss [53].

1.5. Electromagnetic cascades

When a high-energy electron or photon is incident on a thick absorber, it initiates an electromagnetic cascade as pair production and bremsstrahlung generate more electrons and photons with lower energy. The longitudinal development is governed by the high-energy part of the cascade, and therefore scales as the radiation length in the material. Electron energies eventually fall below the critical energy, and then dissipate their energy by ionization and excitation rather than by the generation of more shower particles. In describing shower behavior, it is therefore convenient to introduce the scale variables

$$t = x/X_0 \ , \qquad y = E/E_c \ , \tag{1.33}$$

so that distance is measured in units of radiation length and energy in units of critical energy.

The mean longitudinal profile of the energy deposition in an electromagnetic cascade is reasonably well described by a gamma distribution [57]:

$$\frac{dE}{dt} = E_0\, b\, \frac{(bt)^{a-1}\, e^{-bt}}{\Gamma\,(a)} \tag{1.34}$$

The maximum $t_{\rm max}$ occurs at $(a-1)/b$. We have made fits to shower profiles in elements ranging from carbon to uranium, at energies from 1 GeV to 100 GeV. The energy deposition profiles are well described by Eq. (1.34) with

$$t_{\rm max} = (a-1)\,/b = 1.0 \times \left(\ln y + C_j\right) \ , \qquad j = e, \gamma \ , \tag{1.35}$$

where $C_e = -0.5$ for electron-induced cascades and $C_\gamma = +0.5$ for photon-induced cascades. To use Eq. (1.34), one finds $(a-1)/b$ from Eq. (1.35) and Eq. (1.33), then finds a either by assuming $b \approx 0.5$ or by finding a more accurate value from Fig. 1.20. The results are very similar for the electron number profiles, but there is some dependence on the atomic number of the medium. A similar form for the electron number maximum was obtained by Rossi in the context of his "Approximation B," [2] but with $C_e = -1.0$ and $C_\gamma = -0.5$; we regard this as superseded by the EGS4 result.

The "shower length" $X_s = X_0/b$ is less conveniently parameterized, since b depends upon both Z and incident energy, as shown in Fig. 1.20. As a corollary of this Z dependence, the number of electrons crossing a plane near shower maximum is underestimated using Rossi's approximation for carbon and seriously overestimated for uranium. Essentially the same b values are obtained for incident electrons and photons. For many purposes it is sufficient to take $b \approx 0.5$.

The length of showers initiated by ultra-high energy photons and electrons is somewhat greater than at lower energies since the first

or first few interaction lengths are increased via the mechanisms discussed above.

The gamma function distribution is very flat near the origin, while the EGS4 cascade (or a real cascade) increases more rapidly. As a result Eq. (1.34) fails badly for about the first two radiation lengths; it was necessary to exclude this region in making fits. Because fluctuations are important, Eq. (1.34) should be used only in applications where average behavior is adequate.

The transverse development of electromagnetic showers in different materials scales fairly accurately with the *Molière radius* R_M, given by [59,60]

$$R_M = X_0\, E_s/E_c \ , \tag{1.36}$$

where $E_s \approx 21$ MeV (Table 1.1), and the Rossi definition of E_c is used.

Measurements of the lateral distribution in electromagnetic cascades are shown in Refs. 59 and 60. On the average, only 10% of the energy lies outside the cylinder with radius R_M. About 99% is contained inside of $3.5R_M$, but at this radius and beyond composition effects become important and the scaling with R_M fails. The distributions are characterized by a narrow core, and broaden as the shower develops. They are often represented as the sum of two Gaussians, and Grindhammer [58] describes them with the function

$$f\,(r) = \frac{2r\,R^2}{\left(r^2 + R^2\right)^2} \ , \tag{1.38}$$

where R is a phenomenological function of x/X_0 and $\ln E$.

At high enough energies, the LPM effect (Sec. 1.4.5) reduces the cross sections for bremsstrahlung and pair production, and hence can cause significant elongation of electromagnetic cascades [43].

1.6. Muon energy loss at high energy

At sufficiently high energies, radiative processes become more important than ionization for all charged particles. For muons and pions in materials such as iron, this "critical energy" occurs at several hundred GeV. (There is no simple scaling with particle mass, but for protons the "critical energy" is much, much higher.) Radiative effects dominate the energy loss of energetic muons found in cosmic rays or produced at the newest accelerators. These processes are characterized by small cross sections, hard spectra, large energy fluctuations, and the associated generation of electromagnetic and (in the case of photonuclear interactions) hadronic showers [61–69]. As a consequence, at these energies the treatment of energy loss as a uniform and continuous process is for many purposes inadequate.

It is convenient to write the average rate of muon energy loss as [70]

$$-dE/dx = a\,(E) + b\,(E)\ E \ . \tag{1.39}$$

Here $a(E)$ is the ionization energy loss given by Eq. (1.4), and $b(E)$ is the sum of e^+e^- pair production, bremsstrahlung, and photonuclear contributions. To the approximation that these slowly-varying functions are constant, the mean range x_0 of a muon with initial energy E_0 is given by

$$x_0 \approx (1/b) \ln\left(1 + E_0/E_{\mu c}\right) \ , \tag{1.40}$$

where $E_{\mu c} = a/b$.

The "muon critical energy" $E_{\mu c}$ can be defined more exactly as the energy at which radiative and ionization losses are equal, and can be

found by solving $E_{\mu c} = a(E_{\mu c})/b(E_{\mu c})$. This definition corresponds to the solid-line intersection in Fig. 1.14 of the full *Review*, and is different from the Rossi definition we used for electrons. It serves the same function: below $E_{\mu c}$ ionization losses dominate, and above $E_{\mu c}$ radiative effects dominate. The dependence of $E_{\mu c}$ on atomic number Z is shown in Fig. 1.23 in the full *Review*, but to 3–4% accuracy

$$E_c = \frac{4700 \text{ MeV}}{(Z+1.47)^{0.838}} \text{ (solids, liquids)} , \quad = \frac{7980 \text{ MeV}}{(Z+2.03)^{-0.879}} \text{ (gases)} .$$

The radiative cross sections are expressed as functions of the fractional energy loss ν. The bremsstrahlung cross section goes roughly as $1/\nu$ over most of the range, while for the pair production case the distribution goes as ν^{-3} to ν^{-2} [71]. "Hard" losses are therefore more probable in bremsstrahlung, and in fact energy losses due to pair production may very nearly be treated as continuous. The simulated [69] momentum distribution of an incident 1 TeV/c muon beam after it crosses 3 m of iron is shown in Fig. 1.24 of the full *Review*. The hard bremsstrahlung photons and hadronic debris from photonuclear interactions induce cascades which can obscure muon tracks in detector planes and reduce tracking efficiency [73].

1.7. Cherenkov and transition radiation [74,75,34]

A charged particle radiates if its velocity is greater than the local phase velocity of light (Cherenkov radiation) or if it crosses suddenly from one medium to another with different optical properties (transition radiation). Neither process is important for energy loss, but both are used in high-energy and cosmic-ray physics detectors.

1.7.1. ***Optical Cherenkov radiation***: The angle θ_c of Cherenkov radiation, relative to the particle's direction, for a particle with velocity βc in a medium with index of refraction n is

$$\begin{aligned} \cos\theta_c &= (1/n\beta) \\ \text{or} \quad \tan\theta_c &= \sqrt{\beta^2 n^2 - 1} \\ &\approx \sqrt{2\,(1-1/n\beta)} \quad \text{for small } \theta_c, \textit{e.g.} \text{ in gases.} \end{aligned} \tag{1.41}$$

The threshold velocity β_t is $1/n$, and $\gamma_t = 1/(1-\beta_t^2)^{1/2}$. Therefore, $\beta_t\gamma_t = 1/(2\delta+\delta^2)^{1/2}$, where $\delta = n-1$. Values of δ for various commonly used gases are given as a function of pressure and wavelength in Ref. 76. For values at atmospheric pressure, see Table 6.1. Data for other commonly used materials are given in Ref. 77.

Practical Cherenkov radiator materials are dispersive. Let ω be the photon's frequency, and let $k = 2\pi/\lambda$ be its wavenumber. The photons propage at the group velocity $v_g = d\omega/dk = c/[n(\omega) + \omega(dn/d\omega)]$. In a non-dispersive medium, this simplies to $v_g = c/n$.

In his classical paper, Tamm [78] showed that for dispersive media the radiation is concentrated in a thin conical shell whose vertex is at the moving charge, and whose opening half-angle η is given by

$$\begin{aligned} \cot\eta &= \left[\frac{d}{d\omega}\,(\omega\tan\theta_c)\right]_{\omega_0} \\ &= \left[\tan\theta_c + \beta^2\omega\, n\,(\omega)\,\frac{dn}{d\omega}\cot\theta_c\right]_{\omega_0} , \end{aligned} \tag{1.42}$$

where ω_0 is the central value of the small frequency range under consideration. (See Fig. 27.24.) This cone has a opening half-angle η, and, unless the medium is non-dispersive ($dn/d\omega = 0$), $\theta_c + \eta \neq 90^0$.

The Cherenkov wavefront 'sideslips' along with the particle [79]. This effect may have timing implications for ring imaging Cherenkov counters [80], but it is probably unimportant for most applications.

The number of photons produced per unit path length of a particle with charge ze and per unit energy interval of the photons is

$$\frac{d^2N}{dEdx} = \frac{\alpha z^2}{\hbar c}\sin^2\theta_c = \frac{\alpha^2 z^2}{r_e\, m_e c^2}\left(1 - \frac{1}{\beta^2 n^2\,(E)}\right)$$
$$\approx 370\,\sin^2\theta_c\,(E)\ \ \mathrm{eV}^{-1}\mathrm{cm}^{-1} \qquad (z=1)\ , \qquad (1.43)$$

or, equivalently,

$$\frac{d^2N}{dxd\lambda} = \frac{2\pi\alpha z^2}{\lambda^2}\ \left(1 - \frac{1}{\beta^2 n^2\,(\lambda)}\right)\ . \qquad (1.44)$$

The index of refraction n is a function of photon energy $E = \hbar\omega$, as is the sensitivity of the transducer used to detect the light. For practical use, Eq. (1.43) must be multiplied by the the transducer response function and integrated over the region for which $\beta\, n(\omega) > 1$. Further details are given in the discussion of Cherenkov detectors in the Particle Detectors section (Sec. 31 of this *Review*).

When two particles are close together (lateral separation $\lesssim 1$ wavelength), the electromagnetic fields from the particles may add coherently, affecting the Cherenkov radiation. Because of their opposite charges, the radiation from an e^+e^- pair at close separation is suppressed compared to two independent leptons [81].

1.7.2. *Coherent radio Cherenkov radiation*:

Coherent Cherenkov radiation is produced by many charged particles with a non-zero net charge moving through matter on an approximately common "wavefront"—for example, the electrons and positrons in a high-energy electromagnetic cascade. The signals can be visible above backgrounds for shower energies as low as 10^{17} eV; see Sec. 32.3.2 for more details. The phenomenon is called the Askaryan effect [82]. Near the end of a shower, when typical particle energies are below E_c (but still relativistic), a charge imbalance develops. The photons can Compton-scatter atomic electrons, and positrons can annihilate with atomic electrons to contribute even more photons which can in turn Compton scatter. These processes result in a roughly 20% excess of electrons over positrons in a shower. The net negative charge leads to coherent radio Cherenkov emission. The radiation includes a component from the decellerating charges (as in bremsstrahlung). Because the emission is coherent, the electric field strength is proportional to the shower energy, and the signal power increases as its square. The electric field strength also increases linearly with frequency, up to a maximum frequency determined by the lateral spread of the shower. This cutoff occurs at about 1 GHz in ice, and scales inversely with the Moliere radius. At low frequencies, the radiation is roughly isotropic, but, as the frequency rises toward the cutoff frequency, the radiation becomes increasingly peaked around the Cherenkov angle. The radiation is linearly polarized in the plane containing the shower axis and the photon direction. A measurement of the signal polarization can be used to help determine the shower direction. The characteristics of this radiation have been nicely demonstrated in a series of experiments at SLAC [83]. A detailed discussion of the radiation can be found in Ref. 84.

1.7.3. ***Transition radiation***: The energy radiated when a particle with charge ze crosses the boundary between vacuum and a medium with plasma frequency ω_p is

$$I = \alpha z^2 \gamma \hbar\omega_p/3 \ , \tag{1.45}$$

where

$$\hbar\omega_p = \sqrt{4\pi N_e r_e^3}\ m_e c^2/\alpha = \sqrt{\rho\ (\text{in g/cm}^3)\ \langle Z/A\rangle} \times 28.81\ \text{eV} \ . \tag{1.46}$$

For styrene and similar materials, $\hbar\omega_p \approx 20$ eV; for air it is 0.7 eV.

The number spectrum $dN_\gamma/d(\hbar\omega$ diverges logarithmically at low energies and decreases rapidly for $\hbar\omega/\gamma\hbar\omega_p > 1$. About half the energy is emitted in the range $0.1 \leq \hbar\omega/\gamma\hbar\omega_p \leq 1$. Inevitable absorption in a practical detector removes the divergence. For a particle with $\gamma = 10^3$, the radiated photons are in the soft x-ray range 2 to 40 keV. The γ dependence of the emitted energy thus comes from the hardening of the spectrum rather than from an increased quantum yield.

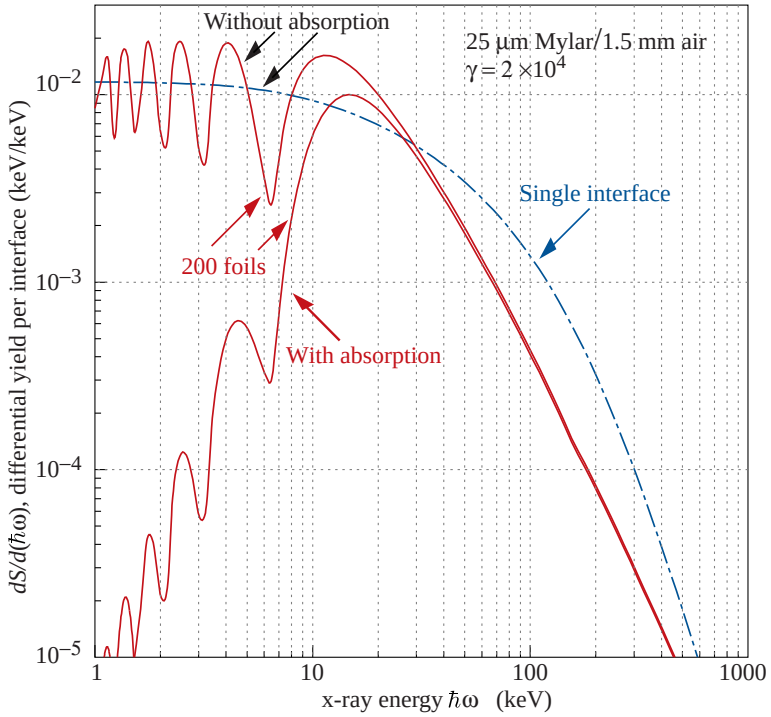

Figure 1.25: X-ray photon energy spectra for a radiator consisting of 200 25 μm thick foils of Mylar with 1.5 mm spacing in air (solid lines) and for a single surface (dashed line). Curves are shown with and without absorption. Adapted from Ref. 85.

The number of photons with energy $\hbar\omega > \hbar\omega_0$ is given by the answer to problem 13.15 in Ref. 34,

$$N_\gamma\,(\hbar\omega > \hbar\omega_0) = \frac{\alpha z^2}{\pi}\left[\left(\ln\frac{\gamma\hbar\omega_p}{\hbar\omega_0} - 1\right)^2 + \frac{\pi^2}{12}\right] \ , \tag{1.47}$$

within corrections of order $(\hbar\omega_0/\gamma\hbar\omega_p)^2$. The number of photons above a fixed energy $\hbar\omega_0 \ll \gamma\hbar\omega_p$ thus grows as $(\ln\gamma)^2$, but the number above a fixed fraction of $\gamma\hbar\omega_p$ (as in the example above) is constant. For example, for $\hbar\omega > \gamma\hbar\omega_p/10$, $N_\gamma = 2.519\,\alpha z^2/\pi = 0.59\% \times z^2$.

The particle stays "in phase" with the x ray over a distance called the formation length, $d(\omega)$. Most of the radiation is produced in a distance $d(\omega) = (2c/\omega)(1/\gamma^2 + \theta^2 + \omega_p^2/\omega^2)^{-1}$. Here θ is the x-ray emission angle, characteristically $1/\gamma$. For $\theta = 1/\gamma$ the formation length has a maximum at $d(\gamma\omega_p/\sqrt{2}) = \gamma c/\sqrt{2}\,\omega_p$. In practical situations it is tens of μm.

Since the useful x-ray yield from a single interface is low, in practical detectors it is enhanced by using a stack of N foil radiators—foils L thick, where L is typically several formation lengths—separated by gas-filled gaps. The amplitudes at successive interfaces interfere to cause oscillations about the single-interface spectrum. At increasing frequencies above the position of the last interference maximum ($L/d(w) = \pi/2$), the formation zones, which have opposite phase, overlap more and more and the spectrum saturates, $dI/d\omega$ approaching zero as $L/d(\omega) \to 0$. This is illustrated in Fig. 1.25 for a realistic detector configuration.

For regular spacing of the layers fairly complicated analytic solutions for the intensity have been obtained [85]. (See also Ref. 86 and references therein.) Although one might expect the intensity of coherent radiation from the stack of foils to be proportional to N^2, the angular dependence of the formation length conspires to make the intensity $\propto N$.

Further discussion and all references may be found in the full *Review of Particle Physics;* the equation and reference numbering corresponds to that version.